INTERNATIONAL JOURNAL FOR NUMERICAL METHODS IN FLUIDS
Int. J. Numer. Meth. Fluids 2006; **50**:649–672
Published online 15 September 2005 in Wiley InterScience (www.interscience.wiley.com). DOI: 10.1002/fld.1054

A 3-D non-hydrostatic pressure model for small amplitude free surface flows

J. W. Lee[1,*,†], M. D. Teubner[1,‡], J. B. Nixon[2,§] and P. M. Gill[1,¶]

[1]*Applied Mathematics, The University of Adelaide, Adelaide, SA 5005, Australia*
[2]*United Water International, GPO Box 1875, Adelaide, SA 5001, Australia*

SUMMARY

A three-dimensional, non-hydrostatic pressure, numerical model with k–ε equations for small amplitude free surface flows is presented. By decomposing the pressure into hydrostatic and non-hydrostatic parts, the numerical model uses an integrated time step with two fractional steps. In the first fractional step the momentum equations are solved without the non-hydrostatic pressure term, using Newton's method in conjunction with the generalized minimal residual (GMRES) method so that most terms can be solved implicitly. This method only needs the product of a Jacobian matrix and a vector rather than the Jacobian matrix itself, limiting the amount of storage and significantly decreasing the overall computational time required. In the second step the pressure–Poisson equation is solved iteratively with a preconditioned linear GMRES method. It is shown that preconditioning reduces the central processing unit (CPU) time dramatically. In order to prevent pressure oscillations which may arise in collocated grid arrangements, transformed velocities are defined at cell faces by interpolating velocities at grid nodes. After the new pressure field is obtained, the intermediate velocities, which are calculated from the previous fractional step, are updated. The newly developed model is verified against analytical solutions, published results, and experimental data, with excellent agreement. Copyright © 2005 John Wiley & Sons, Ltd.

KEY WORDS: non-hydrostatic pressure; Newton–GMRES; preconditioned GMRES; free surface flows; k–ε turbulence model

1. INTRODUCTION

Over the past two decades, three-dimensional (3-D) models, using the hydrostatic pressure approximation [1, 2], have been developed extensively. If this approximation is assumed, the

*Correspondence to: J. W. Lee, Applied Mathematics, The University of Adelaide, Adelaide, SA 5005, Australia.
†E-mail: jong.lee@adelaide.edu.au
‡E-mail: mteubner@maths.adelaide.edu.au
§E-mail: john.nixon@uwi.com.au
¶E-mail: pgill@maths.adelaide.edu.au

Contract/grant sponsor: University of Adelaide
Contract/grant sponsor: United Water International Pty Ltd

Received 18 November 2004
Revised 15 June 2005
Accepted 21 June 2005

vertical momentum equation is omitted and the vertical velocity is calculated from the continuity equation. Such numerical models can be applied to many shallow water flows. However, in some flows in which the ratio of the wave length to the depth is small, this approximation is inaccurate. More recently, as computer power has increased dramatically, a few numerical models have considered the non-hydrostatic pressure by means of solving a pressure related Poisson equation. The numerical techniques for the pressure–Poisson equation are usually either the semi-implicit method for the pressure-linked equation (SIMPLE)-family methods (SIMPLE, [3]; SIMPLER, [4]; SIMPLEC, [5]) or fractional step methods [6–10]. The SIMPLE methods need multiple iterations per time step until the initially guessed pressure field has converged. Alternatively a fractional step method can be employed by separating the pressure into hydrostatic and non-hydrostatic parts, and using time marching computations.

In most non-hydrostatic models for free surface flows [6–9], only parts of the equations are treated implicitly, and then the resulting matrix can be inverted inexpensively. For example, the water surface elevation and the vertical diffusion terms in the momentum equations are discretized implicitly by Casulli [6]. In this way, the velocity field is obtained by inverting a tri-diagonal matrix after the water surface elevation is determined.

In this study, most terms are solved implicitly using Newton's method with an almost matrix-free methodology. For maximum flexibility in the representation of the computational domain, the governing equations are solved in a generalized coordinate system.

2. MATHEMATICAL FORMULATION

The 3-D Navier–Stokes equations with the Boussinesq approximation can be written in conservation form as

$$\frac{\partial u}{\partial x}+\frac{\partial v}{\partial y}+\frac{\partial w}{\partial z}=0 \tag{1}$$

$$\frac{\partial u}{\partial t}+\frac{\partial}{\partial x}(u^2)+\frac{\partial}{\partial y}(uv)+\frac{\partial}{\partial z}(uw)=-\frac{1}{\rho}\frac{\partial P}{\partial x}+\frac{\partial}{\partial x}\left(\nu_{\mathrm{T}}\frac{\partial u}{\partial x}\right)+\frac{\partial}{\partial y}\left(\nu_{\mathrm{T}}\frac{\partial u}{\partial y}\right)+\frac{\partial}{\partial z}\left(\nu_{\mathrm{T}}\frac{\partial u}{\partial z}\right) \tag{2a}$$

$$\frac{\partial v}{\partial t}+\frac{\partial}{\partial x}(uv)+\frac{\partial}{\partial y}(v^2)+\frac{\partial}{\partial z}(vw)=-\frac{1}{\rho}\frac{\partial P}{\partial y}+\frac{\partial}{\partial x}\left(\nu_{\mathrm{T}}\frac{\partial v}{\partial x}\right)+\frac{\partial}{\partial y}\left(\nu_{\mathrm{T}}\frac{\partial v}{\partial y}\right)+\frac{\partial}{\partial z}\left(\nu_{\mathrm{T}}\frac{\partial v}{\partial z}\right) \tag{2b}$$

$$\frac{\partial w}{\partial t}+\frac{\partial}{\partial x}(uw)+\frac{\partial}{\partial y}(vw)+\frac{\partial}{\partial z}(w^2)=-\frac{1}{\rho}\frac{\partial P}{\partial z}-g+\frac{\partial}{\partial x}\left(\nu_{\mathrm{T}}\frac{\partial w}{\partial x}\right)+\frac{\partial}{\partial y}\left(\nu_{\mathrm{T}}\frac{\partial w}{\partial y}\right)+\frac{\partial}{\partial z}\left(\nu_{\mathrm{T}}\frac{\partial w}{\partial z}\right) \tag{2c}$$

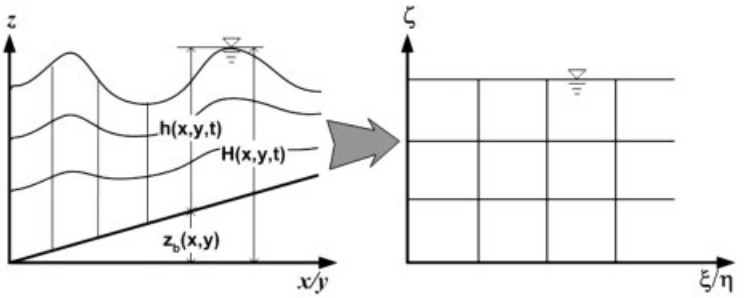

Figure 1. Transformation from Cartesian (x, y, z) to generalized (ξ, η, ζ) coordinates.

where $u(x, y, z, t)$, $v(x, y, z, t)$, and $w(x, y, z, t)$ are mean velocity components in the Cartesian x-, y-, and z-coordinates, respectively, t is time, $P(x, y, z, t)$ is pressure, $v_T(x, y, z, t)$ is turbulent eddy viscosity, ρ is density, assumed to be constant, and g is gravitational acceleration.

For a free surface problem, the continuity equation (1) is integrated from the bottom $z_b(x, y)$ to the surface $H(x, y, t) = h(x, y, t) + z_b(x, y)$ (Figure 1), which yields the free surface equation

$$\frac{\partial h}{\partial t} + \frac{\partial \overline{u}}{\partial x} + \frac{\partial \overline{v}}{\partial y} = 0 \tag{3}$$

where $\overline{u}(x, y, t)$ and $\overline{v}(x, y, t)$ are depth averaged velocities, given by

$$\overline{u} = \int_{z_b}^{H} u \, \mathrm{d}z \quad \text{and} \quad \overline{v} = \int_{z_b}^{H} v \, \mathrm{d}z \tag{4}$$

In many hydrostatic models [1, 2], it is assumed that the pressure varies depending on the amount of water above a point, so that it is a function of water surface elevation only, leading to the hydrostatic approximation [11]. However, in this model the pressure is decomposed into hydrostatic and non-hydrostatic (or hydrodynamic) parts [8] resulting in

$$P = \rho g(H - z) + q \tag{5}$$

where $q(x, y, z, t)$ is the non-hydrostatic pressure.

In order to overcome difficulties arising from free surface movement, the σ-coordinate system [12] has been used widely. In this research we use a similar approach, applying a generalized coordinate transformation from (x, y, z, t) to (ξ, η, ζ, τ) (see Figure 1). Using the approximation (5), the governing equations (1)–(2) are transformed to

$$\frac{\partial}{\partial \xi}\left(\frac{U}{J}\right) + \frac{\partial}{\partial \eta}\left(\frac{V}{J}\right) + \frac{\partial}{\partial \zeta}\left(\frac{W}{J}\right) = 0 \tag{6}$$

$$\frac{\partial \mathbf{Q}}{\partial \tau} + \frac{\partial}{\partial \xi}(\mathbf{E} - \mathbf{E}_\mathrm{v}) + \frac{\partial}{\partial \eta}(\mathbf{F} - \mathbf{F}_\mathrm{v}) + \frac{\partial}{\partial \zeta}(\mathbf{G} - \mathbf{G}_\mathrm{v}) = \mathbf{P}_\mathrm{h} + \mathbf{P}_\mathrm{d} \tag{7}$$

where

$$U = \xi_x u + \xi_y v + \xi_z w, \quad V = \eta_x u + \eta_y v + \eta_z w \quad \text{and} \quad W = \zeta_x u + \zeta_y v + \zeta_z w \tag{8a}$$

are the transformed velocities, J is the Jacobian of the coordinate transformation

$$\mathbf{Q} = \frac{1}{J}\begin{pmatrix} u \\ v \\ w \end{pmatrix}, \quad \mathbf{E} = \frac{U}{J}\begin{pmatrix} u \\ v \\ w \end{pmatrix}, \quad \mathbf{F} = \frac{V}{J}\begin{pmatrix} u \\ v \\ w \end{pmatrix} \quad \text{and} \quad \mathbf{G} = \frac{W + \zeta_t}{J}\begin{pmatrix} u \\ v \\ w \end{pmatrix} \tag{8b}$$

$$\mathbf{P}_{\mathrm{h}} = -g\begin{pmatrix} \left(\frac{\xi_x}{J}H\right)_\xi + \left(\frac{\eta_x}{J}H\right)_\eta + \left(\frac{\zeta_x}{J}H\right)_\zeta \\ \left(\frac{\xi_y}{J}H\right)_\xi + \left(\frac{\eta_y}{J}H\right)_\eta + \left(\frac{\zeta_y}{J}H\right)_\zeta \\ 0 \end{pmatrix} \quad \text{and}$$

$$\mathbf{P}_{\mathrm{d}} = -\frac{1}{\rho}\begin{pmatrix} \left(\frac{\xi_x}{J}q\right)_\xi + \left(\frac{\eta_x}{J}q\right)_\eta + \left(\frac{\zeta_x}{J}q\right)_\zeta \\ \left(\frac{\xi_y}{J}q\right)_\xi + \left(\frac{\eta_y}{J}q\right)_\eta + \left(\frac{\zeta_y}{J}q\right)_\zeta \\ \left(\frac{\xi_z}{J}q\right)_\xi + \left(\frac{\eta_z}{J}q\right)_\eta + \left(\frac{\zeta_z}{J}q\right)_\zeta \end{pmatrix} \tag{8c}$$

represent the hydrostatic and non-hydrostatic pressure terms, respectively, and finally, the viscous terms are given by

$$\mathbf{E}_{\mathrm{v}} = \frac{\nu_{\mathrm{T}}}{J}\left\{\nabla\xi\cdot\nabla\xi\begin{pmatrix} u_\xi \\ v_\xi \\ w_\xi \end{pmatrix} + \nabla\xi\cdot\nabla\eta\begin{pmatrix} u_\eta \\ v_\eta \\ w_\eta \end{pmatrix} + \nabla\xi\cdot\nabla\zeta\begin{pmatrix} u_\zeta \\ v_\zeta \\ w_\zeta \end{pmatrix}\right\}$$

$$\mathbf{F}_{\mathrm{v}} = \frac{\nu_{\mathrm{T}}}{J}\left\{\nabla\xi\cdot\nabla\eta\begin{pmatrix} u_\xi \\ v_\xi \\ w_\xi \end{pmatrix} + \nabla\eta\cdot\nabla\eta\begin{pmatrix} u_\eta \\ v_\eta \\ w_\eta \end{pmatrix} + \nabla\eta\cdot\nabla\zeta\begin{pmatrix} u_\zeta \\ v_\zeta \\ w_\zeta \end{pmatrix}\right\} \tag{8d}$$

$$\mathbf{G}_{\mathrm{v}} = \frac{\nu_{\mathrm{T}}}{J}\left\{\nabla\xi\cdot\nabla\zeta\begin{pmatrix} u_\xi \\ v_\xi \\ w_\xi \end{pmatrix} + \nabla\eta\cdot\nabla\zeta\begin{pmatrix} u_\eta \\ v_\eta \\ w_\eta \end{pmatrix} + \nabla\zeta\cdot\nabla\zeta\begin{pmatrix} u_\zeta \\ v_\zeta \\ w_\zeta \end{pmatrix}\right\}$$

Note that only the vertical grid changes with time, so that ξ_t and η_t do not appear in (7)–(8).

For turbulence modelling, the standard k–ε equations [13] are used. These can be written in vector form as

$$\frac{\partial \breve{\mathbf{Q}}}{\partial \tau} + \frac{\partial}{\partial \xi}(\breve{\mathbf{E}} - \breve{\mathbf{E}}_{\mathrm{v}}) + \frac{\partial}{\partial \eta}(\breve{\mathbf{F}} - \breve{\mathbf{F}}_{\mathrm{v}}) + \frac{\partial}{\partial \zeta}(\breve{\mathbf{G}} - \breve{\mathbf{G}}_{\mathrm{v}}) = \breve{\mathbf{S}} \tag{9}$$

where

$$\breve{\mathbf{Q}} = \frac{1}{J}\begin{pmatrix} k \\ \varepsilon \end{pmatrix}, \quad \breve{\mathbf{E}} = \frac{U}{J}\begin{pmatrix} k \\ \varepsilon \end{pmatrix}, \quad \breve{\mathbf{F}} = \frac{V}{J}\begin{pmatrix} k \\ \varepsilon \end{pmatrix}, \quad \breve{\mathbf{G}} = \frac{W + \zeta_t}{J}\begin{pmatrix} k \\ \varepsilon \end{pmatrix}$$

$$\breve{\mathbf{S}} = \frac{1}{J}\begin{pmatrix} \mathscr{P} - \varepsilon \\ \dfrac{c_{1\varepsilon}\mathscr{P}\varepsilon}{k} - \dfrac{c_{2\varepsilon}\varepsilon^2}{k} \end{pmatrix} \tag{10a}$$

$$\begin{aligned}
\breve{\mathbf{E}}_{\mathrm{v}} &= \frac{\nu_{\mathrm{T}}}{J}\left\{\nabla\xi\cdot\nabla\xi\begin{pmatrix} k_\xi/\sigma_k \\ \varepsilon_\xi/\sigma_\varepsilon \end{pmatrix} + \nabla\xi\cdot\nabla\eta\begin{pmatrix} k_\eta/\sigma_k \\ \varepsilon_\eta/\sigma_\varepsilon \end{pmatrix} + \nabla\xi\cdot\nabla\zeta\begin{pmatrix} k_\zeta/\sigma_k \\ \varepsilon_\zeta/\sigma_\varepsilon \end{pmatrix}\right\} \\
\breve{\mathbf{F}}_{\mathrm{v}} &= \frac{\nu_{\mathrm{T}}}{J}\left\{\nabla\xi\cdot\nabla\eta\begin{pmatrix} k_\xi/\sigma_k \\ \varepsilon_\xi/\sigma_\varepsilon \end{pmatrix} + \nabla\eta\cdot\nabla\eta\begin{pmatrix} k_\eta/\sigma_k \\ \varepsilon_\eta/\sigma_\varepsilon \end{pmatrix} + \nabla\eta\cdot\nabla\zeta\begin{pmatrix} k_\zeta/\sigma_k \\ \varepsilon_\zeta/\sigma_\varepsilon \end{pmatrix}\right\} \\
\breve{\mathbf{G}}_{\mathrm{v}} &= \frac{\nu_{\mathrm{T}}}{J}\left\{\nabla\xi\cdot\nabla\zeta\begin{pmatrix} k_\xi/\sigma_k \\ \varepsilon_\xi/\sigma_\varepsilon \end{pmatrix} + \nabla\eta\cdot\nabla\zeta\begin{pmatrix} k_\eta/\sigma_k \\ \varepsilon_\eta/\sigma_\varepsilon \end{pmatrix} + \nabla\zeta\cdot\nabla\zeta\begin{pmatrix} k_\zeta/\sigma_k \\ \varepsilon_\zeta/\sigma_\varepsilon \end{pmatrix}\right\}
\end{aligned} \tag{10b}$$

$k(x, y, z, t)$ is the turbulent kinetic energy (TKE), $\varepsilon(x, y, z, t)$ is the TKE dissipation rate and $\mathscr{P}$ is the turbulence production. After solving (9)–(10), the turbulent eddy viscosity is determined using

$$\nu_{\mathrm{T}} = c_\mu \frac{k^2}{\varepsilon} \tag{11}$$

The turbulence constants have been found to be $c_\mu = 0.09$, $c_{1\varepsilon} = 1.44$, $c_{2\varepsilon} = 1.92$, $\sigma_k = 1.0$, and $\sigma_\varepsilon = 1.3$ [13].

The surface water equation (3) is transformed into

$$\frac{\partial}{\partial \tau}\left(\frac{h}{J}\right) + \frac{\partial}{\partial \xi}\left(\frac{\overline{U}}{J}\right) + \frac{\partial}{\partial \eta}\left(\frac{\overline{V}}{J}\right) = 0 \tag{12}$$

where $\overline{U} = \xi_x \bar{u} + \xi_y \bar{v}$, and $\overline{V} = \eta_x \bar{u} + \eta_y \bar{v}$.

3. NUMERICAL APPROXIMATION

In the numerical approximation of Equations (6)–(9), all variables except the transformed velocities are defined at grid nodes. The transformed velocities are assigned between nodes (see Figure 2) to yield a grid arrangement similar to that used in References [10, 14], in order

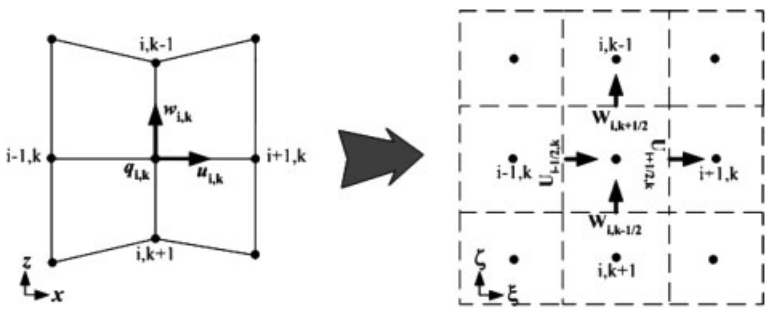

Figure 2. Grid transformation and definition of the transformed velocities.

to prevent a possible checkerboard pressure field [4] at collocated grid points. In Figure 2, i and k denote grid points in the ξ- and ζ-directions with grid spacings $\Delta\xi$ and $\Delta\zeta$, respectively. Variations in the η-direction are represented by the j index with grid spacing $\Delta\eta$.

3.1. Spatial discretization

The symmetric total variation diminishing (TVD) method [15] is used to approximate the inviscid fluxes numerically. By applying this technique, rapid changes in the flow fields can be captured using a three-point stencil in one direction. We define the numerical fluxes at cell faces as

$$\mathbf{E}^*_{i+1/2,j,k} = \tfrac{1}{2}(\mathbf{E}_{i,j,k} + \mathbf{E}_{i+1,j,k}) - \tfrac{1}{2}|U_{i+1/2,j,k}|(1 - \phi_{i+1/2,j,k})\Delta\mathbf{Q}_{i+1/2,j,k} \tag{13}$$

where $\Delta\mathbf{Q}_{i+1/2,j,k} = \mathbf{Q}_{i+1,j,k} - \mathbf{Q}_{i,j,k}$, and $\phi_{i+1/2,j,k}$ is obtained by using the minmod limiter

$$\phi_{i+1/2,j,k} = \text{minmod}(1, r^+) + \text{minmod}(1, r^-) - 1 \tag{14a}$$

where

$$r^+ = \frac{\mathbf{Q}_{i-1/2,j,k}}{\mathbf{Q}_{i+1/2,j,k}}, \quad r^- = \frac{\mathbf{Q}_{i+3/2,j,k}}{\mathbf{Q}_{i+1/2,j,k}} \tag{14b}$$

and the minmod function is defined as

$$\text{minmod}(x, y) = \begin{cases} 0 & \text{for } xy \leqslant 0 \\ x & \text{for } |x| \leqslant |y| \\ y & \text{for } |x| > |y| \end{cases} \tag{14c}$$

Since the Cartesian velocities are defined at grid nodes, U at cell faces is interpolated using these Cartesian velocities. Several interpolation techniques are discussed in Section 3.3.2.

A similar approximation is applied for the η- and ζ-directional fluxes $\mathbf{F}$ and $\mathbf{G}$.

For the hydrostatic and non-hydrostatic pressure terms of (8c) in (7), a second-order central approximation is used.

If the viscous terms $\frac{\partial \mathbf{E}_v}{\partial \xi}$, $\frac{\partial \mathbf{F}_v}{\partial \eta}$ and $\frac{\partial \mathbf{G}_v}{\partial \zeta}$ (where $\mathbf{E}_v$, $\mathbf{F}_v$ and $\mathbf{G}_v$ are defined by (8d)) are expressed in the general form $\frac{\partial}{\partial \xi}(L\frac{\partial M}{\partial \xi})$ and $\frac{\partial}{\partial \xi}(L\frac{\partial M}{\partial \eta})$ for appropriate L and M, these are approximated using

$$\begin{aligned}\frac{\partial}{\partial \xi}\left(L\frac{\partial M}{\partial \xi}\right) &= \frac{1}{(\Delta\xi)^2}[L_{i+1/2,j,k}(M_{i+1,j,k}-M_{i,j,k})-L_{i-1/2,j,k}(M_{i,j,k}-M_{i-1,j,k})]\\ \frac{\partial}{\partial \xi}\left(L\frac{\partial M}{\partial \eta}\right) &= \frac{1}{4\Delta\xi\Delta\eta}[L_{i+1/2,j,k}(M_{i+1,j+1,k}-M_{i+1,j-1,k}+M_{i,j+1,k}-M_{i,j-1,k})\\ &\quad -L_{i-1/2,j,k}(M_{i,j+1,k}-M_{i,j-1,k}+M_{i-1,j+1,k}-M_{i-1,j-1,k})]\end{aligned} \tag{15}$$

3.2. GMRES method

When a linear system of equations, represented by

$$\mathbf{A}\mathbf{x}=\mathbf{b} \tag{16}$$

is solved, the generalized minimal residual (GMRES) method [16] constructs an orthonormal basis of the Krylov subspace, $\mathbf{K}_\mu$, which is defined by

$$\mathbf{K}_\mu = \mathrm{span}\{\mathbf{r}^{(0)}, \mathbf{A}\mathbf{r}^{(0)}, \ldots, \mathbf{A}^{(\mu-1)}\mathbf{r}^{(0)}\} \tag{17}$$

where $\mathbf{r}^{(0)}=\mathbf{b}-\mathbf{A}\mathbf{x}^{(0)}$ is the residual after using an initial guess $\mathbf{x}^{(0)}$, $\mathbf{A}$ is the coefficient, or Jacobian, matrix, and μ is the number of iterations. An approximate solution is found using

$$\mathbf{x}^{(\mu)}=\mathbf{x}^{(0)}+\mathbf{z}^{(\mu)} \quad \text{with} \quad \mathbf{z}^{(\mu)}\in\mathbf{K}_\mu \tag{18}$$

where $\mathbf{z}^{(\mu)}$ is the global minimum of $\mathbf{r}^{(\mu)}$. Using this method, matrices can be inverted whether or not they are symmetric and/or positive definite. However, one of the major limiting aspects of this method is that it can be very slow as the number of iterations increases. To remedy this problem, a modified form uses $\mathbf{r}^{(0)}=\mathbf{r}^{(\mu)}$ and $\mathbf{x}^{(0)}=\mathbf{x}^{(\mu)}$, denoted by GMRES($\mu$) [16]. Moreover, the use of a preconditioning matrix can improve the convergence rate [17]. In this study, however, GMRES(20) is used without preconditioning because convergent solutions are obtained within ten iterations in most cases.

3.3. Time integration

The governing equations are solved using two fractional steps involving hydrostatic and non-hydrostatic pressure, respectively. In the first step, intermediate velocities are estimated using the hydrostatic pressure (and omitting the non-hydrostatic pressure) in the momentum equation (7). In the second step, updated velocities are determined by incorporating the non-hydrostatic pressure.

3.3.1. Hydrostatic step. After dropping the non-hydrostatic pressure terms, (7) can be written as

$$\mathscr{F}(\tilde{\mathbf{Q}})=\frac{\partial \tilde{\mathbf{Q}}}{\partial \tau}+\frac{\partial}{\partial \xi}(\tilde{\mathbf{E}}-\tilde{\mathbf{E}}_v)+\frac{\partial}{\partial \eta}(\tilde{\mathbf{F}}-\tilde{\mathbf{F}}_v)+\frac{\partial}{\partial \zeta}(\tilde{\mathbf{G}}-\tilde{\mathbf{G}}_v)-\tilde{\mathbf{P}}_h=0 \tag{19}$$

where $\mathscr{F}$ is the function representing the momentum equations to be solved, and $\tilde{\mathbf{Q}}$, etc. denote intermediate solutions which are to be modified in the second step by solving for the non-hydrostatic pressure. Substituting (13) and (15) into (19) yields

$$\begin{aligned}\mathscr{F}(\tilde{\mathbf{Q}}) = {} & \frac{\tilde{\mathbf{Q}} - \mathbf{Q}^n}{\Delta\tau} + \frac{\theta}{\Delta\xi}(\tilde{\mathbf{E}}^*_{i+1/2,j,k} - \tilde{\mathbf{E}}^*_{i-1/2,j,k} + \delta\tilde{\mathbf{E}}_{\mathrm{v}}) \\ & + \frac{1-\theta}{\Delta\xi}(\mathbf{E}^*_{i+1/2,j,k} - \mathbf{E}^*_{i-1/2,j,k} + \delta\mathbf{E}_{\mathrm{v}})^n \\ & + \frac{\theta}{\Delta\eta}(\tilde{\mathbf{F}}^*_{i,j+1/2,k} - \tilde{\mathbf{F}}^*_{i,j-1/2,k} + \delta\tilde{\mathbf{F}}_{\mathrm{v}}) \\ & + \frac{1-\theta}{\Delta\eta}(\mathbf{F}^*_{i,j+1/2,k} - \mathbf{F}^*_{i,j-1/2,k} + \delta\mathbf{F}_{\mathrm{v}})^n \\ & + \frac{\theta}{\Delta\zeta}(\tilde{\mathbf{G}}^*_{i,j,k+1/2} - \tilde{\mathbf{G}}^*_{i,j,k-1/2} + \delta\tilde{\mathbf{G}}_{\mathrm{v}}) \\ & + \frac{1-\theta}{\Delta\zeta}(\mathbf{G}^*_{i,j,k+1/2} - \mathbf{G}^*_{i,j,k-1/2} + \delta\mathbf{G}_{\mathrm{v}})^n \\ & - \theta\tilde{\mathbf{P}}_{\mathrm{h}} - (1-\theta)\mathbf{P}^n_{\mathrm{h}} = 0 \end{aligned} \tag{20}$$

where n denotes the time level, $\Delta\tau$ is the time step, and δ represents the second-order discretization of (15), to reduce complexity. We also introduce θ, which controls implicitness and produces the second-order Crank–Nicolson type formula for $\theta = 0.5$, and the first-order backward Euler method for $\theta = 1$. Throughout our applications $\theta = 0.5$ has been used. The hydrostatic term $\mathbf{P}_{\mathrm{h}}$ is an indirect function of $\mathbf{Q}$, and is updated after calculating h from the water surface equation (12); h is updated so that the new water surface can be automatically obtained after the Newton iteration step has converged. By doing this, the surface water equation (12) can be strongly coupled with the momentum equations (7). Introducing a sub-iteration index m for the Newton iterations, (20) can be written as

$$\mathbf{B}(\tilde{\mathbf{Q}}^{m+1} - \tilde{\mathbf{Q}}^m) = -\mathscr{F}(\tilde{\mathbf{Q}}^m, \mathbf{Q}^n) \tag{21}$$

where $\mathbf{B} = \partial\mathscr{F}/\partial\tilde{\mathbf{Q}}^m$. Equation (21) is iterated until $|\tilde{\mathbf{Q}}^{m+1} - \tilde{\mathbf{Q}}^m| \to 0$, $\mathscr{F} \to 0$, or $\mathbf{R}^m(= -\mathbf{B}(\tilde{\mathbf{Q}}^{m+1} - \tilde{\mathbf{Q}}^m) - \mathscr{F}) \to 0$, after which the time step increases from n to $n+1$.

The GMRES method does not use the matrix $\mathbf{B}$ explicitly, but needs only a product of the matrix and a vector (thereby requiring significantly less computer storage). This product can be replaced by the relationship [18]

$$\mathbf{B}\mathbf{v} = \frac{\mathscr{F}(\tilde{\mathbf{Q}} + \varepsilon\mathbf{v}) - \mathscr{F}(\tilde{\mathbf{Q}})}{\varepsilon} \tag{22}$$

where $\mathbf{v}$ is the vector being multiplied, and ε is a carefully chosen small positive parameter. Complicated formulae have been developed for ε [19], but

$$\varepsilon = \frac{\sqrt{\sigma}}{\|\mathbf{v}\|_2} \tag{23}$$

is a simple expression that provides satisfactory accuracy [20], where $\|\mathbf{v}\|_2$ denotes the Euclidean norm of the vector $\mathbf{v}$, and $\sigma = 10^{-14}$ [20] is used for double precision calculations. If $\mathscr{F}(\tilde{\mathbf{Q}})$ is calculated and stored during the previous iteration, (22) needs only one function evaluation. Higher-order difference quotients can be introduced at the expense of more function evaluations [21]. However (22) does not affect the ability to obtain convergent solutions using double precision computations [20].

Even after $\tilde{\mathbf{Q}} = [\tilde{u}, \tilde{v}, \tilde{w}]^{\mathrm{T}}/J$ is obtained, these new, intermediate, velocities may not satisfy the continuity equation. Thus, to develop a divergence-free velocity field, the non-hydrostatic pressure is determined using the continuity equation (6) in the second fractional step. If the hydrostatic pressure approximation is used, the ζ-component of the momentum equation (7) is ignored and the vertical velocity w is obtained by solving the continuity equation (6) and applying (8a).

3.3.2. Non-hydrostatic step. In this step, updated velocities are calculated by considering the non-hydrostatic pressure term, which results in

$$\mathbf{Q}^{n+1} = \tilde{\mathbf{Q}} + \Delta\tau \mathbf{P}_{\mathrm{d}} \tag{24}$$

which can be expanded in component form as

$$\begin{aligned}
\frac{u^{n+1}}{J} &= \frac{\tilde{u}}{J} - \frac{\Delta\tau}{\rho}\left[\left(\frac{\xi_x}{J}q\right)_\xi + \left(\frac{\eta_x}{J}q\right)_\eta + \left(\frac{\zeta_x}{J}q\right)_\zeta\right] \\
\frac{v^{n+1}}{J} &= \frac{\tilde{v}}{J} - \frac{\Delta\tau}{\rho}\left[\left(\frac{\xi_y}{J}q\right)_\xi + \left(\frac{\eta_y}{J}q\right)_\eta + \left(\frac{\zeta_y}{J}q\right)_\zeta\right] \\
\frac{w^{n+1}}{J} &= \frac{\tilde{w}}{J} - \frac{\Delta\tau}{\rho}\left[\left(\frac{\xi_z}{J}q\right)_\xi + \left(\frac{\eta_z}{J}q\right)_\eta + \left(\frac{\zeta_z}{J}q\right)_\zeta\right]
\end{aligned} \tag{25}$$

The relationship between the normal velocities and the non-hydrostatic pressure can be obtained by substituting (25) into (8a), leading to

$$\begin{aligned}
U^{n+1} &= \tilde{U} - \frac{\Delta\tau}{\rho}[(\nabla\xi\cdot\nabla\xi)q_\xi + (\nabla\xi\cdot\nabla\eta)q_\eta + (\nabla\xi\cdot\nabla\zeta)q_\zeta] \\
V^{n+1} &= \tilde{V} - \frac{\Delta\tau}{\rho}[(\nabla\xi\cdot\nabla\eta)q_\xi + (\nabla\eta\cdot\nabla\eta)q_\eta + (\nabla\eta\cdot\nabla\zeta)q_\zeta] \\
W^{n+1} &= \tilde{W} - \frac{\Delta\tau}{\rho}[(\nabla\xi\cdot\nabla\zeta)q_\xi + (\nabla\eta\cdot\nabla\zeta)q_\eta + (\nabla\zeta\cdot\nabla\zeta)q_\zeta]
\end{aligned} \tag{26}$$

where $\tilde{U}$, $\tilde{V}$, and $\tilde{W}$ are the intermediate transformed velocities at the cell faces. Since u, v, and w are defined at the cell centre, interpolation is needed. In this study, three interpolation

techniques are examined. Two of these techniques (two-point linear interpolation and a third-order method [22]) interpolate velocities using variables in the same direction and are thus referred to as single-dimensional interpolation techniques. The third-order method uses the minmod function of the central difference of second-order derivatives. For uniform grids, this third-order method can be written as

$$U_{i+1/2,j,k} = U_{i,j,k} + \tfrac{1}{2}(U_{i+1,j,k} - U_{i,j,k}) - \tfrac{1}{2}\text{minmod}(c_{i,j,k}, c_{i+1,j,k}) \tag{27a}$$

where the minmod function is defined in (14c) and

$$c_{i,j,k} = U_{i+1,j,k} - 2U_{i,j,k} + U_{i-1,j,k} \tag{27b}$$

The third interpolation method averages velocities over three-dimensional space using

$$U_{i+1/2,j,k} = \tfrac{1}{6}(U_{i,j,k} + U_{i+1,j,k} + U_e + U_w + U_t + U_b) \tag{28a}$$

where the multi-dimensionally interpolated velocities are

$$\begin{aligned} U_e &= \tfrac{1}{4}(U_{i,j,k} + U_{i+1,j,k} + U_{i,j+1,k} + U_{i+1,j+1,k}) \\ U_w &= \tfrac{1}{4}(U_{i,j,k} + U_{i+1,j,k} + U_{i,j-1,k} + U_{i+1,j-1,k}) \\ U_t &= \tfrac{1}{4}(U_{i,j,k} + U_{i+1,j,k} + U_{i,j,k+1} + U_{i+1,j,k+1}) \\ U_b &= \tfrac{1}{4}(U_{i,j,k} + U_{i+1,j,k} + U_{i,j,k-1} + U_{i+1,j,k-1}) \end{aligned} \tag{28b}$$

After substituting (26) into (6), the pressure–Poisson equation is obtained. After approximating the second-order derivatives, this elliptic equation yields a 19-diagonal matrix that only contains grid transformation relationships. Listed in the Appendix are the full (A1) and discrete (A2) pressure–Poisson equations. When the water surface changes, the grid transformation relationship varies, even if uniform horizontal grids are used, so that the coefficient matrix is not symmetric. For this reason, the linear system of equations cannot be solved by the conjugate gradient method. However, a diagonally dominant matrix is always produced, so that convergence using iterative methods is guaranteed. A linear version of the GMRES method is used with preconditioning. The linear system (16) with the right preconditioning matrix is

$$\mathbf{A}\mathbf{M}^{-1}\mathbf{x}^* = \mathbf{b} \quad \text{with} \quad \mathbf{x}^* = \mathbf{M}\mathbf{x} \tag{29}$$

where $\mathbf{M}$ is the preconditioner, which should approximate $\mathbf{A}$. The preconditioned matrix $\mathbf{A}\mathbf{M}^{-1}$ has a smaller spectral radius than $\mathbf{A}$, so that extra computation will be compensated for by a faster convergence rate. When $\mathbf{A}$ is expressed as the sum of diagonal ($\hat{\mathbf{D}}$), strictly lower ($\hat{\mathbf{E}}$), and strictly upper ($\hat{\mathbf{F}}$) matrices, it can be factorized as

$$\mathbf{A} = \hat{\mathbf{E}} + \hat{\mathbf{D}} + \hat{\mathbf{F}} = (\hat{\mathbf{E}}\hat{\mathbf{D}}^{-1} + \mathbf{I})(\hat{\mathbf{D}} + \hat{\mathbf{F}}) - \mathscr{E} = \mathbf{L}\mathbf{U} - \mathscr{E} \tag{30}$$

where $\mathscr{E} = \hat{\mathbf{E}}\hat{\mathbf{D}}^{-1}\hat{\mathbf{F}}$ is the error in the above factorization, and $\mathbf{L}$ and $\mathbf{U}$ are, respectively, lower and upper triangular matrices that can be inverted easily by forward and backward substitution. If the $\mathbf{LU}$ matrix is used as a preconditioner (the symmetric Gauss–Seidel (SGS) method), the factorization error is ignored. In 3-D problems, storing the coefficient and preconditioning matrices may require significant capacity. Therefore only non-zero elements are stored, using

the compressed sparse row (CSR) format [23]. The effectiveness of using this preconditioning matrix is discussed in Section 4.1.

After solving the linear system for the non-hydrostatic pressure, the new velocity field, which will be divergence-free, is easily obtained from (25). Using this divergence-free velocity field, the standard k–ε equations (9) are solved with a similar numerical method as used for the momentum equations (7). The surface water equation (12), solved explicitly after defining velocities at cell faces using a 2-D version of (28a), is then solved once more, to account for the effect of the non-hydrostatic pressure.

3.4. Solution procedure

The overall solution procedure is summarized as follows:

(i) Obtain the intermediate velocity field using Newton's method, leading to values for the water surface elevation.
(ii) Interpolate cell-centred velocities to obtain cell-faced values, and solve the new non-hydrostatic pressure field.
(iii) Update the intermediate velocities using (25) to obtain the divergence-free velocity field.
(iv) Calculate k and ε using the velocities obtained from step (iii).
(v) Calculate the new water surface elevation to account for the non-hydrostatic pressure effect, and update the grid variables.

3.5. Boundary conditions

For the non-hydrostatic pressure at wall and open boundaries, a zero normal velocity condition is used rather than specifying the non-hydrostatic pressure. For instance, an impermeable velocity condition is imposed at a wall ($i=1$), so that $U_{-1/2,j,k} = -U_{1/2,j,k}$ [10]. Because of the cross-derivatives, pressures outside the boundaries still need to be specified even after applying this velocity condition. This is performed by a locally one-dimensional second-order extrapolation. At the free surface, the non-hydrostatic pressure is set to zero. Details of inflow boundary conditions are described for each application.

To avoid the requirement of a large number of small grid elements to adequately represent the rapid variation of flow variables near model walls and bottom, a wall function is applied at these boundaries. Using this method, boundary conditions are specified at the first grid point from the wall rather than at the boundary itself. The velocity normal to each wall is set to zero while the two tangential velocities are determined using a method similar to Stansby [8], which is based on the standard formulae for open channel flows [24] given by

$$\frac{u_1}{u_*} = \begin{cases} \dfrac{1}{\kappa}\ln\left(\dfrac{30\bar{z}_1}{k_s}\right) & \text{for rough walls} \\ \dfrac{1}{\kappa}\ln\left(\dfrac{9.05u_*\bar{z}_1}{\nu}\right) & \text{for smooth walls} \end{cases} \tag{31}$$

where u_1 is the velocity parallel to the boundary, which is calculated from the momentum equations (7) at $\bar{z}_1$, $\bar{z}_1$ is the normal distance of the first grid point from the boundary, u_* is the shear velocity, which is related to the bottom shear stress, τ_w, as $u_* = \sqrt{\tau_w/\rho}$; $\kappa = 0.41$ is the von Karman constant; k_s is the roughness height, and ν is the kinematic viscosity. Using

this shear velocity u_*, boundary conditions for k and ε at the wall [13] are

$$k = \frac{u_*^2}{\sqrt{c_\mu}} \quad \text{and} \quad \varepsilon = \frac{|u_*^3|}{\kappa \bar{z}_1} \tag{32}$$

At the free surface, without wind stress, k and ε are obtained [13] from

$$\frac{\partial k}{\partial z} = 0 \quad \text{and} \quad \varepsilon = \frac{(k\sqrt{c_\mu})^{1.5}}{0.07\kappa h} \tag{33}$$

3.6. Grid generation

In this paper, horizontal grids are distributed equally depending on the geometrical boundaries. When inviscid flow or constant eddy viscosity is assumed, the water depth is also divided using an equally spaced vertical grid. For turbulent calculations, however, concentration of vertical grid points near the bottom and surface boundaries is achieved using a grid clustering method similar to that of Hoffmann and Chiang [25], by applying

$$\zeta = \alpha_1 + (1-\alpha_1)\frac{\ln[\{\alpha_2 + (2\alpha_1+1)(z-z_b)/h - 2\alpha_1\}/\{\alpha_2 - (2\alpha_1+1)(z-z_b)/h + 2\alpha_1\}]}{\ln[(\alpha_2+1)/(\alpha_2-1)]} \tag{34}$$

with α_1 and α_2 to control clustering location and density. The inverse of (34) is given by

$$z = z_b + h\frac{(2\alpha_1+\alpha_2)\{(\alpha_2+1)/(\alpha_2-1)\}^{(\zeta-\alpha_1)/(1-\alpha_1)} + 2\alpha_1 - \alpha_2}{(2\alpha_1+1)[1+\{(\alpha_2+1)/(\alpha_2-1)\}^{(\zeta-\alpha_1)/(1-\alpha_1)}]} \tag{35}$$

4. MODEL VALIDATION

In this section, four test cases are examined to verify the numerical model against analytical solutions, published results, and experimental data. These four test cases include inviscid flow of a standing wave in a closed basin (Section 4.1), wind driven circulation with a constant turbulent eddy viscosity (Section 4.2), and two cases involving turbulence in a trench channel (Section 4.3) and a meandering channel (Section 4.4).

4.1. Standing wave in a closed basin

This is one of the most widely used test cases to verify non-hydrostatic pressure models [6, 26] since, by choosing a relatively small wave length λ compared to the depth, the hydrostatic approximation is no longer valid. For comparison purposes, inviscid flow is assumed. For the initial condition, all velocities are set to zero and the water surface elevation is given by

$$H(x) = \eta_0 \cos\left(\frac{2\pi}{\lambda}x\right) + h_0 \quad \text{with} \quad 0 \leqslant x \leqslant l \tag{36}$$

where $\eta_0 = 0.1\,\text{m}$ is the amplitude; $\lambda = 2l$ is the wave length; $l = 10\,\text{m}$ is the domain of the square basin, and $h_0 = 10\,\text{m}$ is the undisturbed water depth. A zero Neumann condition is used for all three velocities at the wall boundaries, while a free slip condition is applied at the free surface.

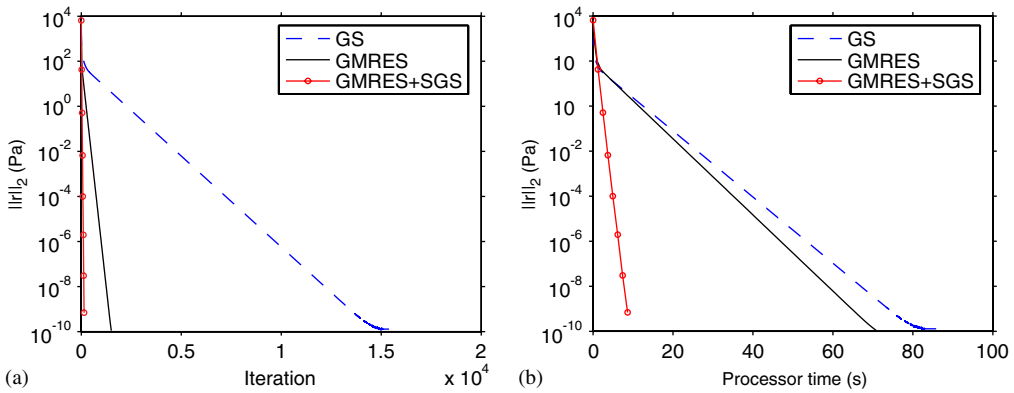

Figure 3. Convergence of three iterative methods, for the standing wave in a closed basin test case: (a) number of iterations against residual (Pa); and (b) processor time (s) against residual (Pa).

Based on small amplitude wave theory [27], the wave celerity c is approximated by

$$c = \sqrt{\frac{g\lambda}{2\pi}\tanh\left(\frac{2\pi}{\lambda}h_0\right)} \tag{37}$$

which is equivalent to $c = 5.57\,\mathrm{m/s}$ so that the wave period T is 3.59 (s). Using the hydrostatic pressure approximation, however, the wave celerity is given by $c = \sqrt{gh_0} = 9.90\,\mathrm{m/s}$ and $T = 2.02\,\mathrm{s}$. Therefore, the sloshing wave of the hydrostatic model will propagate with a faster speed than that of the non-hydrostatic model.

The computational domain uses a constant grid spacing of 0.5 m in the horizontal directions, with 20 layers in the ζ-direction equally divided. A small time step of $\Delta\tau = 0.001\,\mathrm{s}$ is used to obtain highly accurate solutions.

We examine the convergence rate of the pressure–Poisson equation using three iterative methods: the Gauss–Seidel (GS) method and the GMRES(20) method with and without SGS preconditioning. In Figure 3, the y-axis represents the Euclidean norm of the residual ($\mathbf{r} = \mathbf{b} - \mathbf{Ax}$) in Pascals (Pa), plotted against the number of iterations and the processor time in seconds (s) measured using a Pentium III 700 MHz PC with 256 MB RAM. As expected, the GS method converges most slowly, and cannot reduce the residual norm below 10^{-10}. The GMRES method without preconditioning is an improvement over the GS method. However, when it is used with the SGS, the number of iterations is reduced dramatically (Figure 3(a)). Even though extra calculations are needed for the preconditioning matrix, the overall performance is the best using GMRES + SGS (Figure 3(b)).

Before comparing the numerical solutions against analytical solutions, we examine the velocity interpolation methods. In general it has been found that the linear interpolation technique performs similarly to the third-order method. Because of this, only computed pressure fields of the third-order and the multi-dimensional methods have been compared, and are shown in Figure 4 at $y = 5\,\mathrm{m}$ and time $t = T/2\,\mathrm{s}$. Note the oscillations in the pressure field produced by the third-order interpolation, not observed when the multi-dimensional scheme is applied.

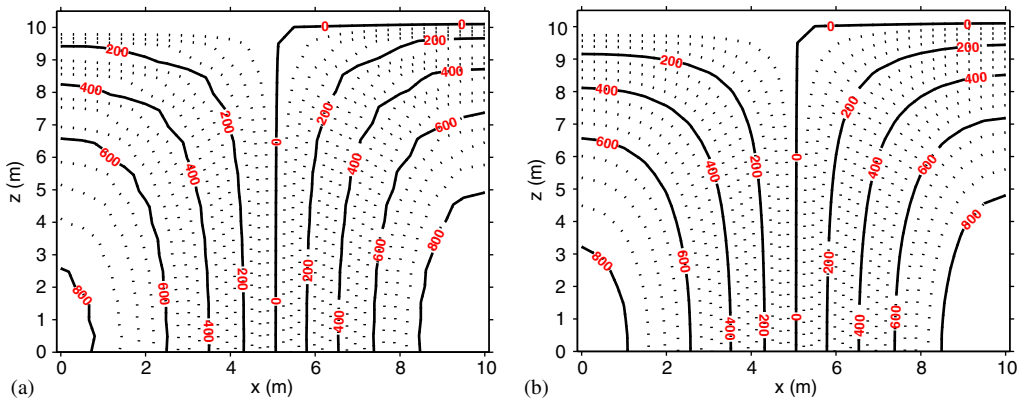

Figure 4. Non-hydrostatic pressure (dashed iso-lines at 50 Pa intervals) at $y = 5$ m and $t = T/2$ s, using two velocity interpolation schemes, for the standing wave in a closed basin test case: (a) using third-order velocity interpolation; and (b) using multi-dimensional velocity interpolation.

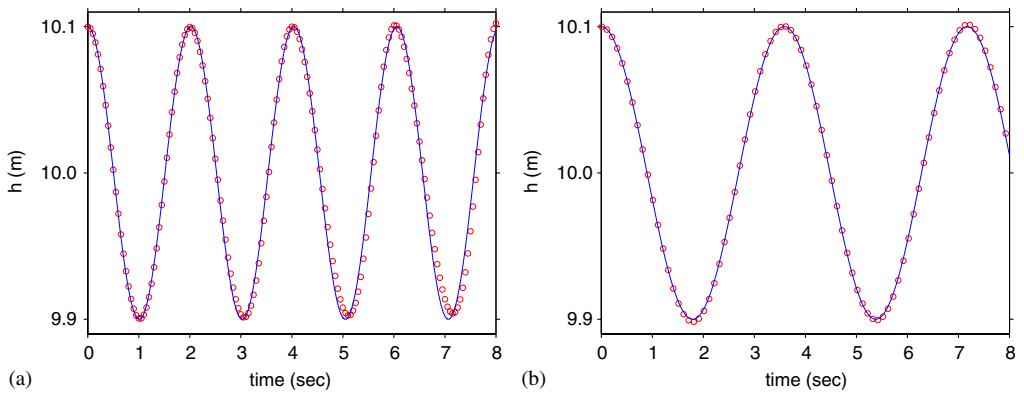

Figure 5. Analytical ($\circ$) and numerical ($-$) water surface elevations (m), at $(x, y) = (0, 5)$ m using the hydrostatic and non-hydrostatic pressure models, for the standing wave in a closed basin test case: (a) hydrostatic pressure models (analytic [7]); and (b) non-hydrostatic pressure models (analytic [27]).

In Figure 5, we present the time history of the water surface elevation h calculated with and without the hydrostatic pressure approximation, at $(x, y) = (0, 5)$ m. Excellent agreement is observed between each analytical solution and its corresponding numerical model. This is despite the fact that, due to the small ratio of the wave length to the depth, the hydrostatic pressure approximation is not valid, and so that the solution with this approximation (Figure 5(b)) is not physically appropriate. Note that the wave periods differ in the two cases because of the differences in the wave celerity.

Figure 6 shows the calculated velocity fields, with and without the hydrostatic pressure approximation, at $y = 5$ m and time $t = T/4$ s. The most significant difference is that the hydrostatic model (Figure 6(a)) calculates much larger vertical velocities near the walls than

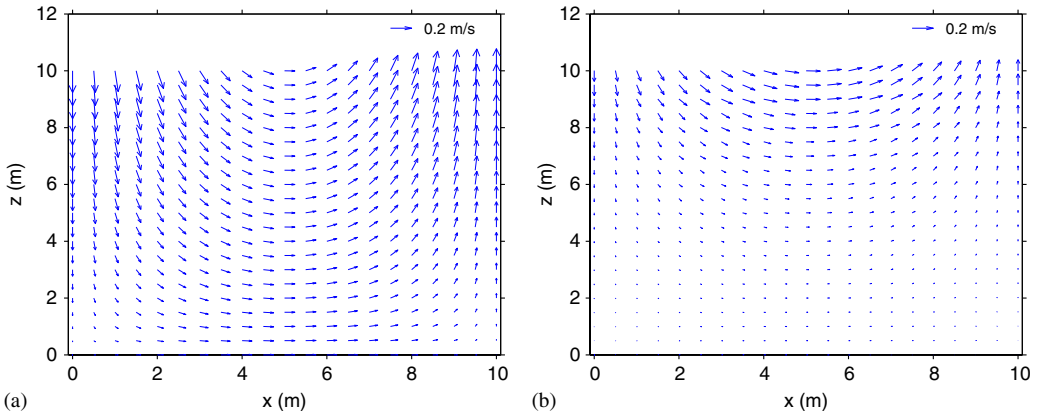

Figure 6. Numerical velocity (m/s) vectors at $y = 5\,\text{m}$ and $t = T/4\,\text{s}$, using the hydrostatic and non-hydrostatic pressure models, for the standing wave in a closed basin test case: (a) hydrostatic pressure model; and (b) non-hydrostatic pressure model.

the non-hydrostatic model (Figure 6(b)). This is because, with the hydrostatic approximation, these velocities are calculated by solving the continuity equation, so that they are only a function of the horizontal velocity field. The results from the hydrostatic model suggest that velocity variations over depth, especially near $x = 5\,\text{m}$, are almost negligible; this is consistent with the shallow water approximation.

The velocity and non-hydrostatic pressure fields, at times $T/8\,\text{s}$ and $5T/8\,\text{s}$, of the numerical solutions are compared with those of the analytical solutions [27] in Figure 7. For $t = T/8\,\text{s}$, the water surface is dropping to the equilibrium position on the left and rising on the right; negative pressure is shown on the left-hand side, while the opposite situation occurs for $t = 5T/8\,\text{s}$. Excellent agreement between these results is clearly indicated.

4.2. *Wind driven circulation*

In this test case, we solve the problem presented in Reference [7] using the same closed basin with a depth of 5 m and a constant wind speed of 10 m/s in the x-direction. All boundary conditions are identical to the previous test case, except at the free surface where a wind shear is applied using the empirical formulae

$$\rho \nu_{\text{T}} \frac{\partial u}{\partial z} = \rho_{\text{a}} c_f u_{\text{w}} |u_{\text{w}}| \quad \text{and} \quad \rho \nu_{\text{T}} \frac{\partial v}{\partial z} = \rho_{\text{a}} c_f v_{\text{w}} |v_{\text{w}}| \tag{38}$$

where ρ_{a} is the density of air; u_{w} ($= 10\,\text{m/s}$) and v_{w} ($= 0\,\text{m/s}$) are wind speeds in the x- and y-directions, respectively, and c_f is the drag coefficient. It is assumed that $\nu_{\text{T}} = 0.001\,\text{m}^2/\text{s}$ and $\rho_{\text{a}} = 1.20\,\text{kg/m}^3$, and that $c_f = 1.5 \times 10^{-3}$ [28]. Computational results are shown in Figure 8 at $y = 5\,\text{m}$ and $t = 1000\,\text{s}$. Even though the hydrostatic pressure model (Figure 8(a)) predicts strong vertical flows near the vertical walls, circulation is observed in the entire basin, while Jankowski's [7] results show strong vertical circulation near the walls only. However, much

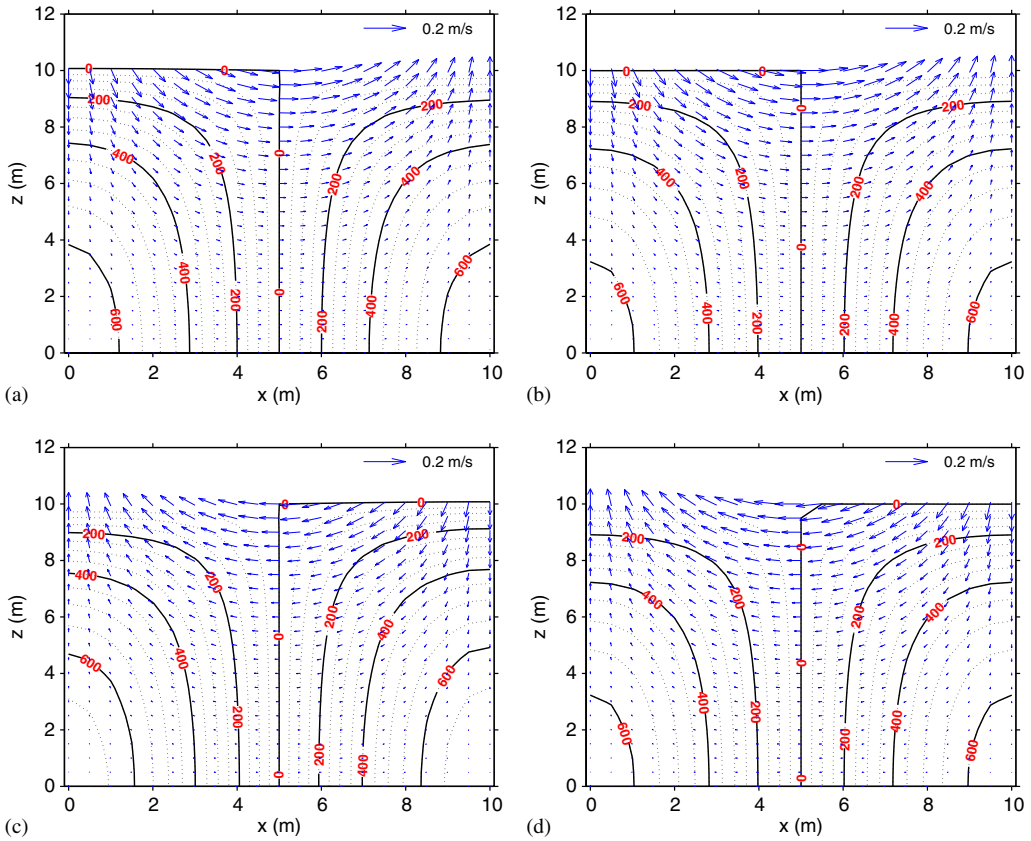

Figure 7. Velocity (m/s) vectors and non-hydrostatic pressure (dashed iso-lines at 50 Pa intervals) at $y = 5$ m from the analytical [27] and numerical solutions at times $T/8$ s and $5T/8$ s, respectively, for the standing wave in a closed basin test case: (a) numerical, at $t = T/8$ s; (b) analytical, at $t = T/8$ s; (c) numerical, at $t = 5T/8$ s; and (d) analytical, at $t = 5T/8$ s.

smoother and more fully developed circulation is obtained in the present non-hydrostatic (Figure 8(a)) and Jankowski [7] models.

4.3. Trench channel flow

In this test case, numerical solutions with the standard k–ε turbulence model are compared with experimental data obtained by van Rijn [29] in a channel 17 m long by 0.5 m wide with 0.7 m high side walls. Similar numerical experiments have been conducted by a number of authors, including Alfrink and van Rijn [30] and Stansby and Zhou [9] without and with a rigid lid approximation, respectively.

The computational domain uses an equally spaced grid of 0.05 m in the longitudinal and lateral directions, with 30 vertical layers using $\alpha_1 = 0.5$ and $\alpha_2 = 1.05$ in (35). To reduce computational requirements, only 2.8 m is considered in the horizontal (x) direction around

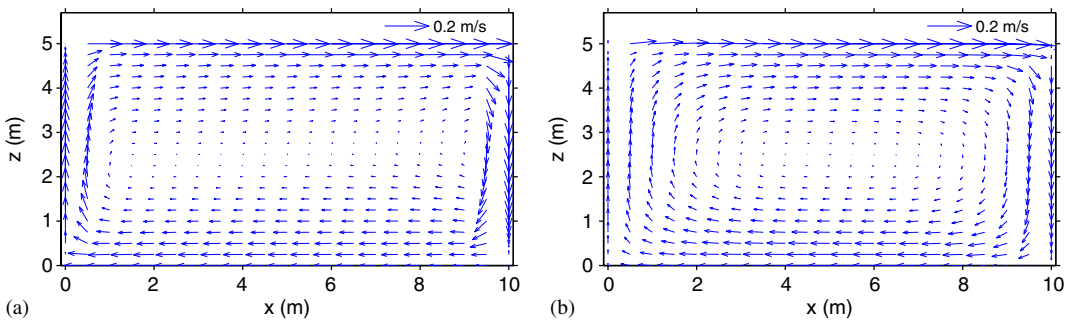

Figure 8. Velocity (m/s) vectors at $y = 5\,\text{m}$ and $t = 1000\,\text{s}$, for the wind driven circulation test case: (a) hydrostatic pressure model; and (b) non-hydrostatic pressure model.

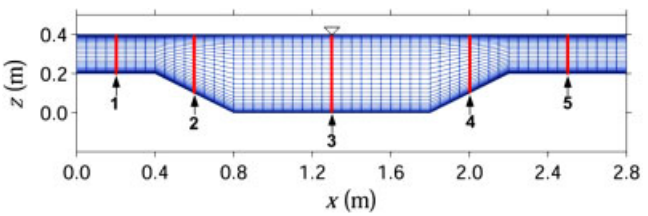

Figure 9. Cross-section through centreline at $y = 0.25\,\text{m}$, with measurement sections and grid distribution of the trench channel flow test case geometry.

the trench. Figure 9 shows a cross-sectional view of the grid distribution along the centre line at $y = 0.25\,\text{m}$. In this figure, five locations indicate where measured data [29] are available. For both the hydrostatic and non-hydrostatic models, a time step of $\Delta\tau = 0.01\,\text{s}$ is used. Residuals showed that steady state solutions were achieved after $t = 50\,\text{s}$ simulation time.

At the left-hand (inflow) boundary, the u velocity is defined using the rough wall condition in (31), and k and ε are specified using (32) with $u_* = 0.03\,\text{m/s}$ [9], while the other velocities are set to zero. At the right-hand (outflow) boundary, the water surface elevation H is specified as 0.4 m, and other independent valuables are described using the zero flux derivatives with respect to the normal direction of the outflow boundary. Along the side walls u, w, k, and ε satisfy the zero flux condition across the wall, while v is zero.

Streamlines computed from the hydrostatic and non-hydrostatic models are compared in Figure 10. Results from these models are very similar, but a slightly smoother circulation pattern near the beginning of the trench is observed for the non-hydrostatic model (Figure 10(b)) compared to the hydrostatic model (Figure 10(a)).

Figure 11 shows the computed and experimentally observed horizontal velocity (u), TKE (k), and shear stress (τ_{xz}), indicating that the overall agreement is excellent in both models, although numerical results from the non-hydrostatic model are slightly more accurate than those from the hydrostatic model. Compared with other standard k–ε models [9, 30] the current model accurately predicts u, k, and τ_{xz}, especially at location 2 where weak circulation occurs leading to negative velocities near the bottom.

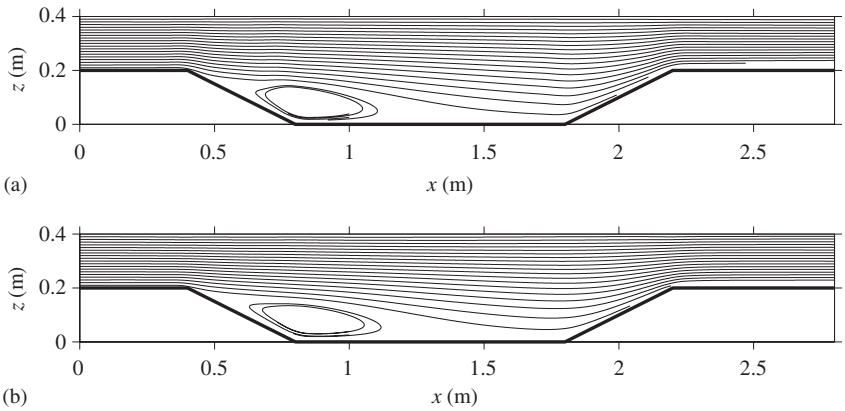

Figure 10. Cross-section through centre line at $y = 0.25$ m of numerical solution streamlines, for the trench channel flow test case: (a) hydrostatic pressure model; and (b) non-hydrostatic pressure model.

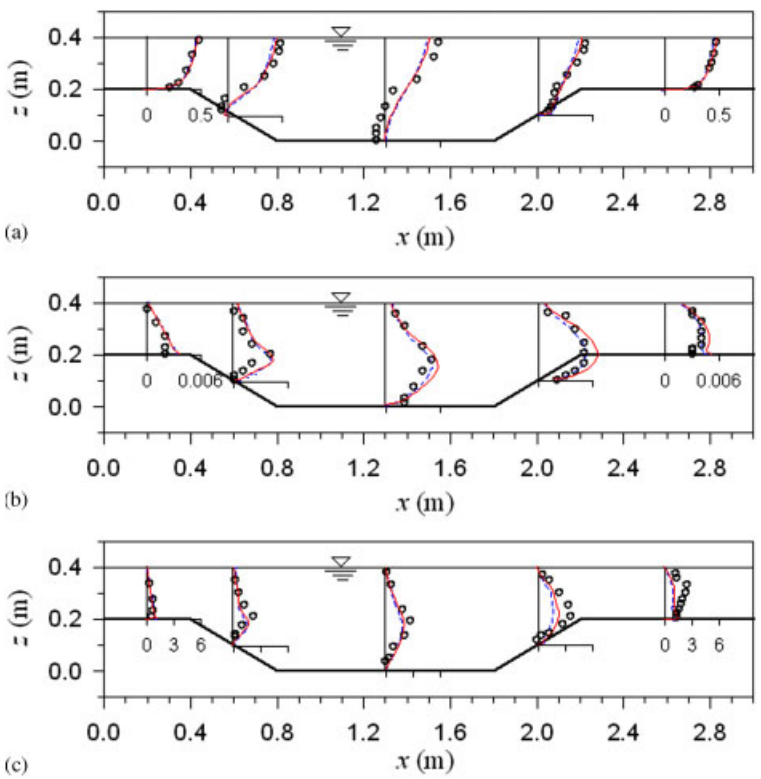

Figure 11. Cross-section through centre line at $y = 0.25$ m of u (m/s), k (m^2/s^2), and τ_{xz} (N/s^2), as computed (hydrostatic pressure model: $--$, non-hydrostatic pressure model: —) and experimentally observed (○) [29], for the trench channel flow test case: (a) u (m/s); (b) k (m^2/s^2); and (c) τ_{xz} (N/m^2).

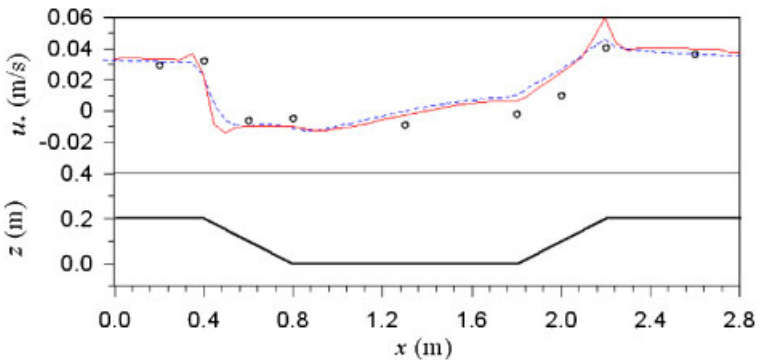

Figure 12. Cross-section through centre line at $y = 0.25$ m of shear velocities (m/s) as computed (hydrostatic pressure model: ––, non-hydrostatic pressure model: —) and experimentally observed (○) [29], for the trench channel flow test case.

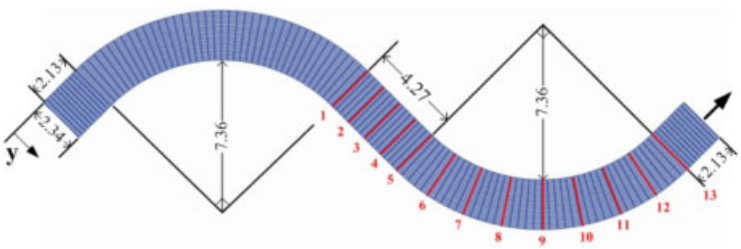

Figure 13. Cross-section through the horizontal plane, with measurement sections and grid distribution, of the meandering channel test case geometry with channel width of 2.34 m.

In Figure 12, the shear velocities along the bottom, u_*, computed from both models using (31), are compared with experimental data [29]. Better experimental agreement is again achieved using the non-hydrostatic model compared to the hydrostatic model. However, the results of both numerical models indicate better accuracy than results from the rigid lid computations of Alfrink and van Rijn [30].

4.4. Meandering channel flow

The meandering channel flow problem has been examined experimentally by Chang [31], and numerically using a rigid lid approximation [32] and a free surface condition [33]. We have simulated this problem using the computational grid shown in Figure 13, where a variable grid has been used in the longitudinal direction, a constant grid, using 0.078 m intervals, in the transverse direction, and a variable grid, using (35) with $\alpha_1 = 0.5$ and $\alpha_2 = 1.1$, in the vertical direction; this gives a total of $116 \times 30 \times 20$ nodes. Figure 13 also shows the locations of the measurement sections presented in Reference [31]. The inflow boundary conditions used

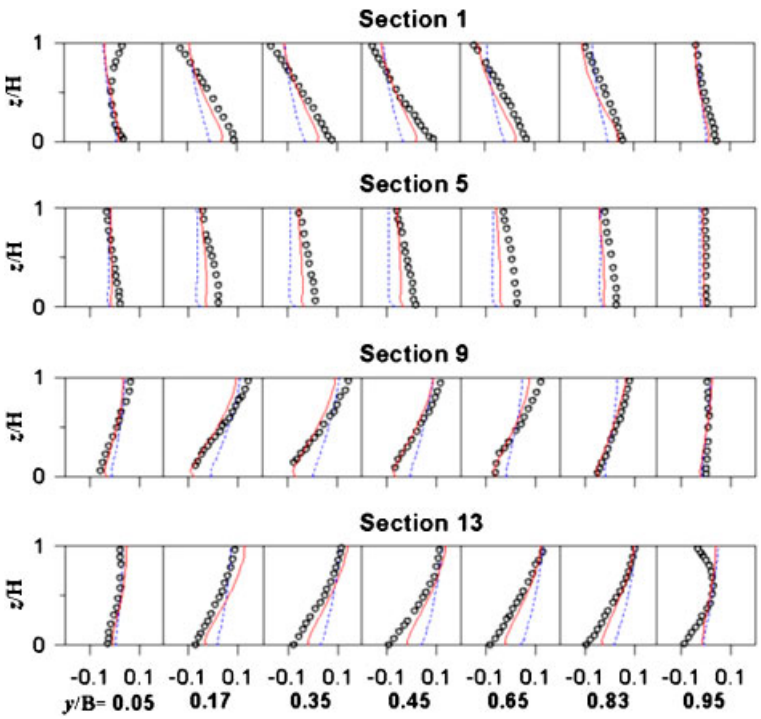

Figure 14. Vertical cross-sections, through selected sections, of transverse velocities v/U_o, as computed (hydrostatic model: ––, non-hydrostatic model: —) and experimentally observed (○, [31]), for the meandering channel test case with channel width of $B = 2.34\,\text{m}$.

are: $U = U_o = 0.355\,\text{m/s}$ [32], and $V = W = 0\,\text{m/s}$. The water surface elevation is specified at the outflow boundary as $H = 0.115\,\text{m}$. The smooth wall boundary condition (31) is applied along the bottom and side walls. In this test, a time increment of $\Delta\tau = 0.02\,\text{s}$ is used, and steady state solutions are considered after 100 s (when residuals indicated steady state had been reached).

In Figure 14, transverse velocities v/U_o computed from the hydrostatic and non-hydrostatic models are compared with experimental data [31] at sections 1, 5, 9, and 13. At the exit of the first bend (section 1), strong currents from the inner to the outer bank near the water surface are observed and computed; these currents are compensated by inverse directional flows near the bottom. At the end of the middle straight channel (section 5), no circulation is observed or computed. Secondary currents, similar in magnitude but in a different direction to those observed and computed at section 1, are observed and computed at section 9. Based on the measured data, there is reverse circulation near the surface at the inner bank of section 13 and the outer bank of section 1. However, the present numerical models fail to predict this small motion. As mentioned in Reference [33], this inaccuracy may be improved by using a more complicated turbulence model.

In general, overall predictions using the non-hydrostatic model are in greater agreement with the experimental data than those using the rigid lid model [32]. The predictions of the non-hydrostatic model are an improvement on those of the hydrostatic model. However, solutions computed using the hydrostatic model do not agree well with the experimental data in this test case, unlike the trench channel flow test case of Section 4.3. This suggests that numerical models without non-hydrostatic pressure may not predict vertical variations of flow variables accurately.

5. CONCLUSION

In this paper, a 3-D numerical model with and without the hydrostatic approximation is presented using a generalized coordinate system. Time integration is performed by two fractional steps. In the hydrostatic fractional step, the intermediate velocity field is solved using a Newton–GMRES method. By considering the non-hydrostatic pressure and the continuity equation, the intermediate velocities are updated to the divergence-free velocities in the non-hydrostatic step. In this second step, the pressure–Poisson equation is solved using the GMRES method with SGS preconditioning. It has been shown that a multi-dimensional velocity interpolation method can prevent oscillating pressure fields that may result from the use of linear or third-order single-dimensional interpolation methods. The newly developed model has been tested using four test cases and compared with analytical solutions, published results, and experimental data. It is shown in calculations without turbulence that the hydrostatic approximation is valid only in certain cases where wave length is relatively long. In test cases involving turbulence, both models can predict mean flow variables quite accurately. However, it is found that the differences in the numerical solutions of the hydrostatic and non-hydrostatic models are noticeable for the meandering channel test case, where complicated vertical motions are observed.

APPENDIX A

The pressure–Poisson equation, obtained by substituting (26) into (6) leads to

$$(\alpha_1 q_\xi + \alpha_2 q_\eta + \alpha_3 q_\zeta)_\xi + (\alpha_4 q_\xi + \alpha_5 q_\eta + \alpha_6 q_\zeta)_\eta + (\alpha_7 q_\xi + \alpha_8 q_\eta + \alpha_9 q_\zeta)_\zeta = \frac{\rho}{\Delta\tau}\left[\left(\frac{\tilde{U}}{J}\right)_\xi + \left(\frac{\tilde{V}}{J}\right)_\eta + \left(\frac{\tilde{W}}{J}\right)_\zeta\right] \tag{A1}$$

where

$$\alpha_1 = (\xi_x^2 + \xi_y^2 + \xi_z^2)/J, \quad \alpha_2 = (\xi_x\eta_x + \xi_y\eta_y + \xi_z\eta_z)/J, \quad \alpha_3 = (\xi_x\zeta_x + \xi_y\zeta_y + \xi_z\zeta_z)/J$$

$$\alpha_4 = (\xi_x\eta_x + \xi_y\eta_y + \xi_z\eta_z)/J, \quad \alpha_5 = (\eta_x^2 + \eta_y^2 + \eta_z^2)/J, \quad \alpha_6 = (\eta_x\zeta_x + \eta_y\zeta_y + \eta_z\zeta_z)/J$$

$$\alpha_7 = (\xi_x\zeta_x + \xi_y\zeta_y + \xi_z\zeta_z)/J, \quad \alpha_8 = (\eta_x\zeta_x + \eta_y\zeta_y + \eta_z\zeta_z)/J, \quad \alpha_9 = (\zeta_x^2 + \zeta_y^2 + \zeta_z^2)/J$$

When (15) is used for the second-order derivatives of the non-hydrostatic pressure, it yields the linear system of equations

$$\begin{aligned}&\beta_1 q_{i-1,j-1,k}+\beta_2 q_{i-1,j,k-1}+\beta_3 q_{i-1,j,k}+\beta_4 q_{i-1,j,k+1}+\beta_5 q_{i-1,j+1,k}\\&+\beta_6 q_{i,j-1,k-1}+\beta_7 q_{i,j-1,k}+\beta_8 q_{i,j-1,k+1}+\beta_9 q_{i,j,k-1}+\beta_{10} q_{i,j,k}\\&+\beta_{11} q_{i,j,k+1}+\beta_{12} q_{i,j+1,k-1}+\beta_{13} q_{i,j+1,k}+\beta_{14} q_{i,j+1,k+1}+\beta_{15} q_{i+1,j-1,k}\\&+\beta_{16} q_{i+1,j,k-1}+\beta_{17} q_{i+1,j,k}+\beta_{18} q_{i+1,j,k+1}+\beta_{19} q_{i+1,j+1,k}=\text{RHS of (A1)}\end{aligned}\tag{A2}$$

where the coefficients are:

$$\beta_1=\frac{1}{4\Delta\xi\Delta\eta}[(\alpha_2)_{i-1/2,j,k}+(\alpha_4)_{i,j-1/2,k}],\quad \beta_2=\frac{1}{4\Delta\xi\Delta\zeta}[(\alpha_3)_{i-1/2,j,k}+(\alpha_7)_{i,j,k-1/2}]$$

$$\beta_4=-\frac{1}{4\Delta\xi\Delta\zeta}[(\alpha_3)_{i-1/2,j,k}+(\alpha_7)_{i,j,k+1/2}],\quad \beta_5=-\frac{1}{4\Delta\xi\Delta\eta}[(\alpha_2)_{i-1/2,j,k}+(\alpha_4)_{i,j+1/2,k}]$$

$$\beta_6=\frac{1}{4\Delta\eta\Delta\zeta}[(\alpha_6)_{i,j-1/2,k}+(\alpha_8)_{i,j,k-1/2}],\quad \beta_8=-\frac{1}{4\Delta\eta\Delta\zeta}[(\alpha_6)_{i,j-1/2,k}+(\alpha_8)_{i,j,k+1/2}]$$

$$\beta_{12}=-\frac{1}{4\Delta\eta\Delta\zeta}[(\alpha_6)_{i,j+1/2,k}+(\alpha_8)_{i,j,k-1/2}],\quad \beta_{14}=\frac{1}{4\Delta\eta\Delta\zeta}[(\alpha_6)_{i,j+1/2,k}+(\alpha_8)_{i,j,k+1/2}]$$

$$\beta_{15}=-\frac{1}{4\Delta\xi\Delta\eta}[(\alpha_2)_{i+1/2,j,k}+(\alpha_4)_{i,j-1/2,k}],\quad \beta_{16}=-\frac{1}{4\Delta\xi\Delta\zeta}[(\alpha_3)_{i+1/2,j,k}+(\alpha_7)_{i,j,k-1/2}]$$

$$\beta_{18}=\frac{1}{4\Delta\xi\Delta\zeta}[(\alpha_3)_{i+1/2,j,k}+(\alpha_7)_{i,j,k+1/2}],\quad \beta_{19}=\frac{1}{4\Delta\xi\Delta\eta}[(\alpha_2)_{i+1/2,j,k}+(\alpha_4)_{i,j+1/2,k}]$$

$$\begin{aligned}\beta_3=&\frac{(\alpha_1)_{i-1/2,j,k}}{\Delta\xi^2}+\frac{1}{4\Delta\xi\Delta\eta}[(\alpha_4)_{i,j-1/2,k}-(\alpha_4)_{i,j+1/2,k}]\\&+\frac{1}{4\Delta\xi\Delta\zeta}[(\alpha_7)_{i,j,k-1/2}-(\alpha_7)_{i,j,k+1/2}]\end{aligned}$$

$$\begin{aligned}\beta_7=&\frac{1}{4\Delta\xi\Delta\eta}[(\alpha_2)_{i-1/2,j,k}-(\alpha_2)_{i+1/2,j,k}]+\frac{(\alpha_5)_{i,j-1/2,k}}{\Delta\eta^2}\\&+\frac{1}{4\Delta\eta\Delta\zeta}[(\alpha_8)_{i,j,k-1/2}-(\alpha_8)_{i,j,k+1/2}]\end{aligned}$$

$$\begin{aligned}\beta_9=&\frac{1}{4\Delta\xi\Delta\zeta}[(\alpha_3)_{i-1/2,j,k}-(\alpha_3)_{i+1/2,j,k}]+\frac{1}{4\Delta\eta\Delta\zeta}[(\alpha_6)_{i,j-1/2,k}-(\alpha_6)_{i,j+1/2,k}]\\&+\frac{(\alpha_9)_{i,j,k-1/2}}{\Delta\zeta^2}\end{aligned}$$

$$\beta_{10}=-\frac{1}{\Delta\xi^2}[(\alpha_1)_{i+1/2,j,k}+(\alpha_1)_{i-1/2,j,k}]-\frac{1}{\Delta\eta^2}[(\alpha_5)_{i,j+1/2,k}+(\alpha_5)_{i,j-1/2,k}]$$

$$-\frac{1}{\Delta\zeta^2}[(\alpha_9)_{i,j,k+1/2}+(\alpha_9)_{i,j,k-1/2}]$$

$$\beta_{11}=\frac{1}{4\Delta\xi\Delta\zeta}[(\alpha_3)_{i+1/2,j,k}-(\alpha_3)_{i-1/2,j,k}]+\frac{1}{4\Delta\eta\Delta\zeta}[(\alpha_6)_{i,j+1/2,k}-(\alpha_6)_{i,j-1/2,k}]$$

$$+\frac{(\alpha_9)_{i,j,k+1/2}}{\Delta\zeta^2}$$

$$\beta_{13}=\frac{1}{4\Delta\xi\Delta\eta}[(\alpha_2)_{i+1/2,j,k}-(\alpha_2)_{i-1/2,j,k}]+\frac{(\alpha_5)_{i,j+1/2,k}}{\Delta\eta^2}$$

$$+\frac{1}{4\Delta\eta\Delta\zeta}[(\alpha_8)_{i,j,k+1/2}-(\alpha_8)_{i,j,k-1/2}]$$

and

$$\beta_{17}=\frac{(\alpha_1)_{i+1/2,j,k}}{\Delta\xi^2}+\frac{1}{4\Delta\xi\Delta\eta}[(\alpha_4)_{i,j+1/2,k}-(\alpha_4)_{i,j-1/2,k}]$$

$$+\frac{1}{4\Delta\xi\Delta\zeta}[(\alpha_7)_{i,j,k+1/2}-(\alpha_7)_{i,j,k-1/2}]$$

ACKNOWLEDGEMENTS

Jong Wook Lee has been supported by an international postgraduate research scholarship (IPRS) from the University of Adelaide and a supplementary scholarship from United Water International Pty Ltd, Adelaide.

REFERENCES

1. Huang W, Spaulding M. 3D model of estuarine circulation and water quality induced by surface discharges. *Journal of Hydraulic Engineering* 1995; **121**:300–311. http://dx.doi.org/10.1061/(ASCE)0733-9429(1995)121:4(300)
2. Lu Q, Wai OWH. An efficient operator splitting scheme for three-dimensional hydrodynamic computations. *International Journal for Numerical Methods in Fluids* 1998; **26**:771–789. http://dx.doi.org/10.1002/(SICI)1097-0363(19980415)26:7<771::AID-FLD672>3.0.CO;2-7
3. Patankar SV, Spalding DB. A calculation procedure for heat, mass and momentum transfer in three-dimensional parabolic flows. *International Journal of Heat and Mass Transfer* 1972; **15**:1787–1806.
4. Patankar SV. *Numerical Heat Transfer and Fluid Flow*. McGraw-Hill: New York, 1980.
5. van Doormaal JP, Raithby GD. Enhancements of the SIMPLE method for predicting incompressible fluid flows. *Numerical Heat Transfer* 1984; **7**:147–163.
6. Casulli V. A semi-implicit finite difference method for non-hydrostatic, free-surface flows. *International Journal for Numerical Methods in Fluids* 1999; **30**:425–440. http://dx.doi.org/10.1002/(SICI)1097-0363(19990630)30:4<425::AID-FLD847>3.0.CO;2-D
7. Jankowski JA. A non-hydrostatic model for free surface flows. *Ph.D. Thesis*, Hanover University, Germany, 1999.
8. Stansby PK. Semi-implicit finite volume shallow-water flow and solute transport solver with k–ε turbulence model. *International Journal for Numerical Methods in Fluids* 1997; **25**:285–313. http://dx.doi.org/10.1002/(SICI)1097-0363(19970815)25:3<285::AID-FLD552>3.0.CO;2-Q
9. Stansby PK, Zhou JG. Shallow-water flow solver with non-hydrostatic pressure: 2D vertical plane problems. *International Journal for Numerical Methods in Fluids* 1998; **28**:541–563. http://dx.doi.org/10.1002/(SICI)1097-0363(19980915)28:3<541::AID-FLD738>3.0.CO;2-0

10. Zang Y, Street RL, Koseff JR. A non-staggered grid, fractional step method for time-dependent incompressible Navier–Stokes equations in curvilinear coordinates. *Journal of Computational Physics* 1994; **114**:18–33. http://dx.doi.org/10.1006/jcph.1994.1146
11. Vreugdenhil CB. *Numerical Methods for Shallow-Water Flow*. Kluwer: Dordrecht, 1994.
12. Phillips NA. A coordinate system having some special advantages for numerical forecasting. *Journal of Meteorology* 1957; **14**:184–185.
13. Rodi W. *Turbulence Models and their Application in Hydraulics—A State of the Art Review*. IAHR: 1984.
14. Kim D, Choi H. A second-order time-accurate finite volume method for unsteady incompressible flow on hybrid unstructured grids. *Journal of Computational Physics* 2000; **162**:411–428. http://dx.doi.org/10.1006/jcph.2000.6546
15. Yee HC. Construction of explicit and implicit symmetric TVD schemes and their applications. *Journal of Computational Physics* 1987; **68**:151–179. http://dx.doi.org/10.1016/0021-9991(87)90049-0
16. Saad Y, Schultz MH. GMRES: a generalized minimal residual algorithm for solving nonsymmetric linear systems. *SIAM Journal on Scientific and Statistical Computing* 1986; **7**:856–869.
17. Rogers SE. Comparison of implicit schemes for the incompressible Navier–Stokes equations. *AIAA Journal* 1995; **33**:2066–2072.
18. Brown PN, Hindmarsh AC. Matrix-free methods for stiff systems of ODEs. *SIAM Journal on Numerical Analysis* 1986; **23**:610–638. http://links.jstor.org/sici?sici=0036-1429%28198606%2923%3A3%3C610%3AMMFSSO%3E2.0.CO%3B2-D
19. Brown PN, Saad Y. Hybrid Krylov methods for nonlinear systems of equations. *SIAM Journal on Scientific and Statistical Computing* 1990; **11**:450–481.
20. Qin N, Ludlow DK, Shaw ST. A matrix-free preconditioned Newton/GMRES method for unsteady Navier–Stokes solutions. *International Journal for Numerical Methods in Fluids* 2000; **33**:223–248. http://dx.doi.org/10.1002/(SICI)1097-0363(20000530)33:2<223::AID-FLD10>3.0.CO;2-V
21. Pernice M, Walker HF. NITSOL: a Newton iterative solver for nonlinear systems. *SIAM Journal on Scientific and Statistical Computing* 1998; **19**:302–318.
22. Kobayashi MH, Pereira JCF. A comparison of second-order convection discretization schemes for incompressible fluid flow. *Communications in Numerical Methods in Engineering* 1996; **12**:395–411. http://dx.doi.org/10.1002/(SICI)1099-0887(199607)12:7<395::AID-CNM987>3.0.CO;2-V
23. Saad Y. *Numerical Methods for Large Eigenvalue Problems* (*Algorithms and Architectures for Advanced Scientific Computing*). Wiley: New York, 1992.
24. Chow VT. *Open-Channel Hydraulics*. McGraw-Hill: New York, 1959.
25. Hoffmann KA, Chiang ST. *Computational Fluid Dynamics for Engineers*, *Volume II*. Engineering Education System: 1993.
26. Koçyigit MB, Falconer RA, Lin B. Three-dimensional numerical modelling of free surface flows with non-hydrostatic pressure. *International Journal for Numerical Methods in Fluids* 2002; **40**:1145–1162. http://dx.doi.org/10.1002/fld.376
27. Dean RG, Dalrymple RA. *Water Wave Mechanics for Engineers and Scientists*. World Scientific: Singapore, 1991.
28. Fischer HB, List EH, Koh RCY, Imberger J, Brooks NH. *Mixing in Inland and Coastal Waters*. Academic Press: New York, 1979.
29. van Rijn LC. *The Computation of the Flow and Turbulence Field in Dredged Trenches*. Delft Hydraulics Laboratory: Delft, 1982.
30. Alfrink BJ, van Rijn LC. Two-equation turbulence model for flow in trenches. *Journal of Hydrologic Engineering* 1983; **109**:941–958.
31. Chang YC. Lateral mixing in meandering channels. *Ph.D. Thesis*, University of Iowa, Iowa.
32. Demuren AO, Rodi W. Calculation of flow and pollutant dispersion in meandering channels. *Journal of Fluid Mechanics* 1986; **172**:63–92.
33. Ye J, McCorquodale JA. Simulation of curved open channel flows by 3D hydrodynamic model. *Journal of Hydrologic Engineering* 1998; **124**:687–698. http://dx.doi.org/10.1061/(ASCE)0733-9429(1998)124:7(687)

